nature nanotechnology

ARTICLES

https://doi.org/10.1038/s41565-019-0398-x

Simultaneous voltage and current density imaging of flowing electrons in two dimensions

Lior Ella[1], Asaf Rozen[1], John Birkbeck[2,3], Moshe Ben-Shalom[2,3,4], David Perello[2,3], Johanna Zultak[2,3], Takashi Taniguchi[5], Kenji Watanabe[5], Andre K. Geim[2,3], Shahal Ilani[1] and Joseph A. Sulpizio[1*]

A variety of physical phenomena associated with nanoscale electron transport often results in non-trivial spatial voltage and current patterns, particularly in nonlocal transport regimes. While numerous techniques have been devised to image electron flows, the need remains for a nanoscale probe capable of simultaneously imaging current and voltage distributions with high sensitivity and minimal invasiveness, in a magnetic field, across a broad range of temperatures and beneath an insulating surface. Here we present a technique for spatially mapping electron flows based on a nanotube single-electron transistor, which achieves high sensitivity for both voltage and current imaging. In a series of experiments using high-mobility graphene devices, we demonstrate the ability of our technique to visualize local aspects of intrinsically nonlocal transport, as in ballistic flows, which are not easily resolvable via existing methods. This technique should aid in understanding the physics of two-dimensional electronic devices and enable new classes of experiments that image electron flow through buried nanostructures in the quantum and interaction-dominated regimes.

Over the past few decades, a growing variety of materials and devices have emerged with electron flow described outside the framework of semi-classical diffusive transport. In these systems, electrons propagate either ballistically through the bulk[1], ballistically via edge transport, such as in topological insulators[2,3], or most recently, collectively via hydrodynamic flow arising from strong electron–electron interactions[4]. In such non-diffusive flows, the relation between current and voltage is no longer local, and the spatial structure of both the current and voltage can take non-trivial forms.

Our understanding of electron flow in two-dimensional systems predominantly stems from transport measurements on lithographically defined devices, which are an indispensable tool in studying many aspects of non-diffusive flows. Such measurements sample the electrochemical potential only at discrete points in space, typically along the edge of a device. However, as noted long ago by Landauer[5], such measurements also have inherent limitations: since transport measurements use fixed voltage probes that sample the potential only at discrete spatial points, they cannot provide a full map of the current and voltage distribution. Furthermore, in the ballistic regime where the electron mean free path is large compared to the probe and device dimensions, such fixed probes sample the electronic distribution in a manner that depends on their geometric details and often disrupt the flow they are aiming to measure[1,6,7]. These limitations illustrate the need for a non-invasive local probe that can provide real-space visualization of the fundamental properties of electronic transport; namely, the electrostatic potential and current density in real space and particularly in regimes where some combination of quantum, ballistic and electron–electron interaction effects becomes dominant.

Several scanning probe techniques have been previously developed that separately image voltage[8–12] or current[13–18] in two-dimensional systems, each with specific advantages, although the emerging classes of materials can benefit from a probe with a broader scope of measurement capabilities. A highly desirable feature for a voltage imaging tool is the ability to image electrons buried beneath insulating surfaces (currently achieved by a Kelvin probe[12] and optical methods[9,11]), due to their increasing prevalence for improving mobility. However, if such a probe aims to address delicate low-energy physics phenomena, it must also possess high voltage sensitivity (currently obtained only with scanning tunnelling potentiometry[8]). Furthermore, it must be able to image across a wide temperature range to capture a broad array of phenomena, and do so non-invasively at small carrier densities and energy scales. Along with the voltage, one would ideally like to image simultaneously the local current density flowing through a device as well. Several techniques have recently excelled in imaging current by measuring the magnetic field it produces (scanning superconducting quantum interference devices (SQUIDS)[13–15,19] and nitrogen vacancy centres[17,18]), although they are limited to operate under small externally applied magnetic fields. Additional scanning techniques (scanning gate microscopy[20,21], near-field scanning optical microscopy[22,23], photocurrent[24], optical[25,26] and microwave impedance[27,28]) have proven crucial for visualizing other aspects of transport through devices. A promising candidate for imaging the properties of flowing electrons is the scanning single-electron transistor (SET)[29–31], owing to its extreme voltage sensitivity. In the past, SETs have been used primarily for imaging equilibrium properties (for example, workfunction and electronic compressibility) and for resolving questions about the spatial distribution of quantum Hall edge states[32]. Their possible capacity to image voltage drops and current density of flowing electrons has remained unexplored.

In this work, we demonstrate a new technique employing nanotube-based SETs[31,33] to simultaneously image the voltage drop and the current distribution of flowing electrons in two dimensions. The technique has nanoscale spatial resolution (~100 nm) and microvolt voltage sensitivity, operates from cryogenic temperatures up to room temperature and at large magnetic fields, and is minimally

[1]Department of Condensed Matter Physics, Weizmann Institute of Science, Rehovot, Israel. [2]School of Physics and Astronomy, University of Manchester, Manchester, UK. [3]National Graphene Institute, University of Manchester, Manchester, UK. [4]School of Physics and Astronomy, Tel Aviv University, Tel Aviv, Israel. [5]National Institute for Materials Science, Tsukuba, Japan. *e-mail: joseph.sulpizio@weizmann.ac.il

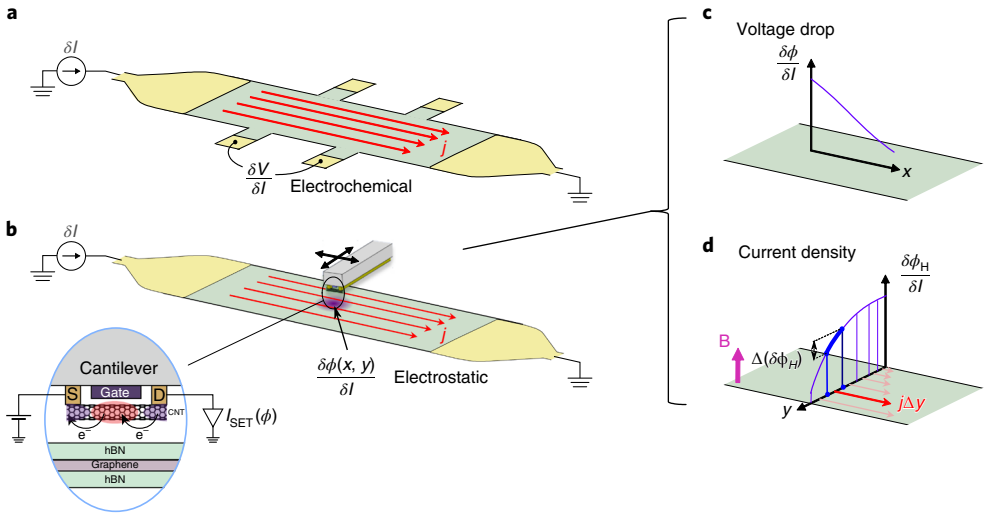

Fig. 1 | Overview of the nanoscale voltage and current imaging technique. a, Conventional transport measurement: alternating current, δI (current density j, red arrows), is passed between the outer contacts (yellow) of a Hall bar device (green). The electrochemical potential difference (δV) between pairs of contacts at the edge of the Hall bar is measured to infer the resistivity and Hall voltage at fixed spatial positions. **b**, Illustration of the SET-based imaging technique. In contrast to the fixed position data obtained by conventional transport measurements, a nanotube-based SET (inset) positioned at the end of a scanning probe cantilever is rastered (black arrows) to image the electrostatic potential (voltage drop), $\delta\varphi(x,y)$, at every spatial position in a device generated by the flowing electrons with total alternating current, δI. Inset, side view of the SET and schematic of the devices imaged in this paper—hBN/graphene heterostructures atop Si/SiO_2. The SET consists of a pristine carbon nanotube, nano-assembled[33] on top of source and drain contacts (yellow) and suspended above a gate electrode (purple), positioned near the edge of the cantilever. At cryogenic temperatures, a quantum dot forms in the suspended segment (red) separated by p–n junctions from hole-doped nanotube leads (blue). The current flowing through the nanotube (black arrows) depends strongly on the electrostatic potential induced by the sample via Coulomb blockade physics, allowing measurement of the local voltage with extreme sensitivity. Note that during operation, no electrons are transferred between the SET and the device under study, and no mechanical force is applied, enabling the measurement of buried electronic devices with minimum disturbance. The technique allows simultaneous imaging of two basic quantities. **c**, Voltage drop of flowing electrons $\delta\phi/\delta I$ (normalized by total current), obtained directly by measuring the local electrostatic potential in sync with the flowing current. While the figure illustrates the drop along the channel, in practice we measure the voltage drop in both spatial directions. **d**, Current density: adding a small perpendicular magnetic field, $\pm B$ (purple), generates a local Hall voltage, $\delta\phi_H(x,y)$ (see main text for definition), without modifying the flow pattern of the current. By measuring the Hall voltage that drops between any two points in the sample, $\Delta(\delta\phi_H)$, (for example, blue points in sketch), together with the local density, $n(x,y)$, we directly obtain the current flowing between these two points, $j\Delta y = \frac{ne}{B}\Delta(\delta\phi_H)$, where e is the electron charge. More generically, we can get a full map of the local current density (magnitude and direction) via $\mathbf{j} = \frac{ne}{B}\hat{\mathbf{z}} \times \nabla(\delta\phi_H)$ (where $\hat{z}$ is a unit vector perpendicular to the plane).

invasive to the flow, making it especially suitable for visualizing non-diffusive transport. We benchmark the technique by mapping electron flow in high-mobility graphene/hexagonal boron nitride (hBN) devices[34]. We observe the evolution from diffusive flow, in which electrostatic potential falls gradually along the device, to ballistic flow, where it drops sharply at its contacts. Independently, we show how the SET can be used to image current streamlines, and how such voltage and current maps can show detailed information about electron flow in the bulk of a device, which is difficult to obtain via conventional methods. Finally, we spatially image the nonlocal, negative voltage distribution associated with ballistic flow. The demonstrated technique enables the imaging of non-diffusive flow phenomena in a variety of buried nanostructures created from a growing list of novel materials and devices.

Overview of nanoscale imaging technique

The principle behind our measurement technique is shown schematically in Fig. 1. In a typical transport measurement (Fig. 1a), fixed, lithographically defined contact electrodes patterned along the perimeter of a device are used to measure the electrochemical voltage drop in response to a flowing current, yielding both the longitudinal (ρ_{xx}) and Hall (ρ_{xy}) resistivities. While these quantities are well-defined locally for diffusive transport, in ballistic flow the contact electrodes sample only the electrons with momenta directed toward them[1,7], yielding an averaged electrochemical potential that depends on the contact orientation and precise geometry. Additionally, such contacts emit thermalized electrons, thereby randomizing their direction, and thus can interfere with the flow. Our technique replaces the fixed voltage probes with a scanning SET, which can non-invasively sample the local, out-of-equilibrium electrostatic potential anywhere in space. The SET couples capacitively to the region in the sample above which it is scanning, so that the local potential of the sample strongly modulates the current passing through it[29–31]. By monitoring the SET current as it scans across the sample under study, we can thus isolate the electrostatic potential, $\delta\phi$, generated in response to an applied total alternating current, δI (Fig. 1b). The measured quantity $\delta\phi/\delta I$, has units of resistance and captures the local change in electrostatic potential (voltage drop) due to the flowing electrons[6,7,35] (Supplementary Information 5).

Analogous to ρ_{xx} and ρ_{xy} conventionally measured in transport, the quantity $\delta\phi/\delta I$ allows us to map in real space two independent properties of a device under study: if measured at zero magnetic field, it gives the voltage drop associated with varying longitudinal resistivity, dropping more sharply in locations that are more resistive (Fig. 1c). Under the application of a weak perpendicular magnetic field $\pm B$, we independently resolve the Hall voltage associated with the flow, $\delta\phi_H/\delta I \equiv (\delta\phi_{+B} - \delta\phi_{-B})/2\delta I$ (Fig. 1d). Since the difference in Hall voltage between two spatial points separated by Δy is directly related to the current passing between them via $j\Delta y = \frac{ne}{B}\Delta(\delta\phi_H)$ (where j and n are the local current and carrier densities and e is the

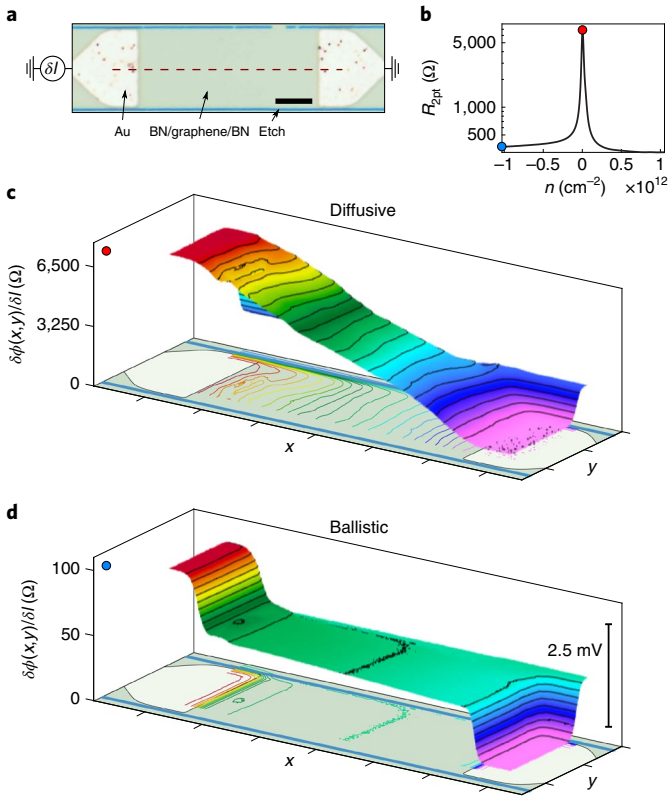

Fig. 2 | Spatial imaging of the voltage drop of flowing electrons in the diffusive and ballistic regimes. a, An optical image of the device, consisting of a conducting mesoscopic channel defined in a single-layer graphene/hBN sandwich (green), using chemically etched boundaries (blue). The current, δI, is passed between a pair of gold contacts (yellow). **b**, Two-probe resistance (R_{2pt}) of the device at $T = 4$ K, measured as a function of carrier density (tuned via back-gate voltage). **c**, Diffusive transport imaged near charge neutrality (red dot, **b**) where the graphene resistivity across the bulk of the device is dominant. The imaged electrostatic potential is shown, normalized by the total current, $\delta\phi(x,y)/\delta I$ (units of resistance). The bottom plane shows the equipotential contours superimposed on the schematic of the graphene channel and contacts, indicating that the voltage drops gradually between the contacts, with some local deviations due to increased disorder near charge neutrality. **d**, Ballistic transport imaged at a hole density of 1×10^{12} cm^{-2} (blue dot, **b**). The voltage drops in a step-like manner at the interface between the contacts and the graphene channel, and is rather flat across the bulk of the device. The total voltage applied across the device in this measurement is ~2.5 mV (side bar).

electron charge), spatially resolved measurement of $\delta\phi_H/\delta I$ directly yields a map of the local current density.

Imaging the voltage drop of flowing electrons

We demonstrate the ability of our technique to image the voltage drop of flowing electrons using a high-mobility graphene/hBN device at a temperature of $T = 4$ K. The graphene is patterned into a channel 11 μm wide (W) and 25 μm long (L) (Fig. 2a), with source and drain contacts exhibiting a typical two-point resistance that is sharply peaked as the carrier density is tuned near charge neutrality via the back-gate voltage (Fig. 2b). The spatial map of the electrostatic potential of the flowing electrons taken at charge neutrality (Fig. 2c) exhibits an overall linear drop along the channel, indicating diffusive behaviour, although with clear local fluctuations reflecting disorder-induced resistivity variations. From the slope of this voltage drop, we find the transport mean free path[36] $l_{tr} = \frac{h}{2e^2 k_F W}\frac{\Delta x}{\Delta(\frac{\delta\phi}{\delta I})}$ to be 0.9 μm, which, as expected for diffusive transport, is much smaller than the device dimensions (h is Planck's constant and k_F is the Fermi wavelength, which we estimate from the residual density fluctuations at charge neutrality). Similar imaging of diffusive flow has been done previously using Kelvin probe microscopy under the application of a high bias voltage[37] (~2 V). The extreme sensitivity of our scanning SET allows us to perform these measurements with three orders of magnitude smaller bias (2.5 mV) that, combined with higher mobility samples and cryogenic temperatures, allows us to access the regime of ballistic flow[10,21,38,39]. Indeed, when we image the voltage drop for a hole density of $n = 1\times10^{12}$ cm^{-2} we measure a strikingly different map that strongly resembles the textbook picture of ballistic transport[7] (Fig. 2d). Here, the resistance is localized almost entirely at the graphene–contact interface, as visualized by the sharp, step-like voltage drops. In the bulk of the device, the electrostatic potential is nearly flat, with only a small, residual drop due to the large but finite mean free path $l_{tr} = 26$ μm.

The spatial maps of $\delta\phi/\delta I$ allow us to quantitatively distinguish the different contributions to the total resistance of the channel. Figure 3a shows the electrostatic potential measured along the centre of the device (dashed line, Fig. 2a) at three carrier densities for both holes and electrons. In the bulk of the device, the potential drop is highly electron–hole symmetric (Fig. 3a, between vertical dashed lines), with resistivity decreasing as density is increased. The contact resistance (Fig. 3a, vertical arrow), however, exhibits a marked electron–hole asymmetry[36]. This is shown systematically in Figs. 3b,c, where the extracted bulk conductivity, σ_{xx}, and contact resistance, $R_{contact}$, are plotted as a function of the carrier density. The larger contact resistance for holes most likely arises from the formation of p–n junctions between the hole-doped graphene bulk and electron-doped regions near the contacts due to differences in the workfunction. For electron doping, where no p–n junctions should form, we can compare against the Sharvin resistance[40] of an ideal contact. We find that the imaged $R_{contact}$ at high electron density approaches the predicted Sharvin value for four-fold spin/valley degenerate fermions in graphene, $R_{Sharvin} = \frac{h\pi}{4e^2 W k_F}$ (Fig. 3d, dashed line), to within a factor of two, indicating large contact transparency (up to transmission ~0.5, top inset Fig. 3c). In Supplementary Information 7, we show an additional example in which we image electron flow around an obstacle, showing electrostatic potential maps in the bulk of a sample that would be challenging to obtain with existing techniques.

Imaging the electron current distribution

To image the local current distribution, we turn to mapping the Hall voltage in real space. We use a second graphene device with a bend geometry (Fig. 4a). In this case, we expect the Hall voltage to reflect the fact that the current follows the bend. Figure 4b,c shows these voltages imaged at small positive and negative perpendicular magnetic fields $B = \pm 20$ mT. Notably, the equipotential lines are now tilted with respect to the channel direction, due to the addition of the Hall voltage to the longitudinal voltage drop. By subtracting these two voltage maps, we remove the longitudinal resistance, which is symmetric in B, isolating the contribution of the Hall voltage, $\delta\phi_H/\delta I$, normalized by the current. To interpret this Hall voltage map, we first note that the density across the channel is nearly constant. We determine this by imaging with the SET the local density of states along the y axis of the graphene device (Fig. 4d), and observing from the variation in the charge neutrality point that the spatial fluctuation in charge density is at most $\delta n_{disorder} \approx 3\times10^9$ cm^{-2}, a small fraction of the average density, $n = -1.1\times10^{11}$ cm^{-2}. If local density variations were present, they could be similarly measured by the SET, making the technique applicable to non-uniform devices as well. Since the Hall electric field must locally balance the Lorentz force, the Hall voltage map, together with the density, allows us to directly obtain the electron flow streamline function[1,41], $\delta\psi = \frac{ne}{B}\delta\phi_H$, whose derivative gives the local current density, $\mathbf{j} = \hat{\mathbf{z}}\times\nabla\delta\psi$. In Fig. 4e we plot

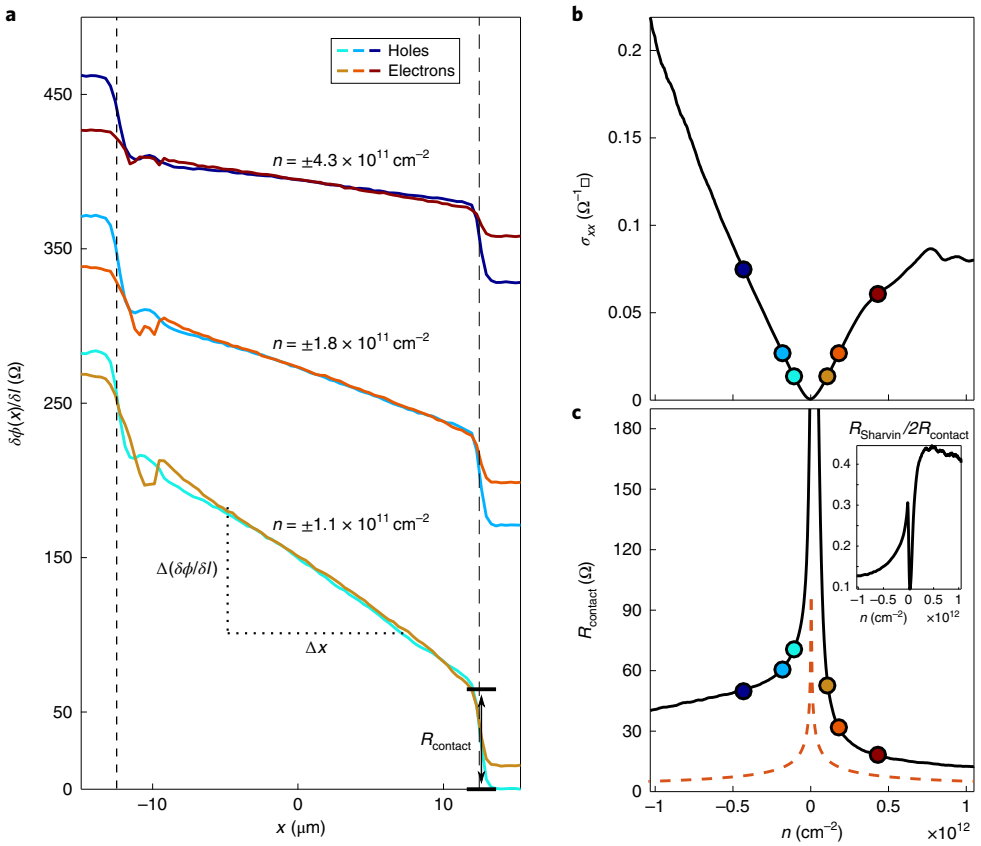

Fig. 3 | Extracting local quantities from electrostatic potential maps. a, Line traces of the imaged voltage drop of the flowing electrons, $\delta\phi/\delta I$, as a function of the spatial coordinate along the centre of the channel, x (dashed line, in Fig. 2a). Measurements are taken at three pairs of equal electron/hole carrier densities. A vertical offset between equal density pairs is added for clarity. The bulk graphene resistivity is determined directly from the local slope of the voltage, normalized by the width of the channel (W) via $\rho_{xx} = W\Delta(\delta\phi/\delta I)/\Delta x$. Notably, at the same carrier density the measured local slopes for electrons and holes are similar. The contact resistance $R_{contact}$ is defined as the size of the $\delta\phi/\delta I$ step between the contacts and the onset of the bulk voltage slope (indicated by black bars), and shows a large degree of electron/hold asymmetry. Near the left contact there is a localized voltage artefact that resulted from voltage cycling of the back-gate, which locally disrupted the operation of the SET. **b**,**c**, Graphene conductivity σ_{xx} and contact resistance extracted from electrostatic potential traces as in **a**, but measured as a continuous function of carrier density. Coloured circles correspond to line cuts in **a**. The orange dashed line in **c** corresponds to the predicted Sharvin contact resistance limit. Inset, deduced contact transparency.

the resulting streamlines (accumulated current is labelled) superimposed on the independently measured zero-field equipotential contours, showing that the current streamlines clearly snake around the bend in the device. We can additionally determine the total current through the device using our imaging technique, independently of transport measurements via $\delta I_{imaged} = \delta\psi(y = W) - \delta\psi(0)$, where y is the coordinate along the channel profile. Indeed, we find that $\delta I_{imaged} = 3.4 \pm 0.2\,\mu A$ matches well the total current $\delta I = 3.2\,\mu A$ measured via transport with no free parameters. The smearing of the streamlines near the channel edges is related to the finite spatial resolution, which is limited by the probe–sample separation in this specific measurement (Supplementary Information 1). The generality of this technique for extracting the current density is discussed in Supplementary Information 6.

Examining the electron flow more closely, we note a sharp increase in resistance at the entrance to the bend, as indicated by the bunching together of the equipotential contours. Diffusive flow with homogenous bulk conductivity should in fact show a resistance decrease at the bend, since there the channel width increases. This is indeed predicted by a simulation of diffusive flow for this exact device geometry (Fig. 4f). For ballistic flow, on the other hand, a change of channel width acts as a reflecting barrier, leading to a resistance increase. An electron billiards simulation of ballistic flow with diffusive boundaries for this device geometry (Fig. 4g) shows a clear bunching of the equipotential contours around the bend as in the experiment, albeit with a reduced resistance increase. The remaining discrepancy can be due to additional disorder and mechanical stress near the etched boundaries, as well as strong electric fields near the etched corners. These detailed maps of both the voltage and current around the bend highlight the advantage of our technique for visualizing the flow inside the bulk of the sample, which is otherwise challenging to obtain via existing techniques.

Visualization of nonlocal electron flow phenomena

As an example of the ability to spatially image nonlocal transport phenomena, we image the ballistic voltage distribution that develops across a paired channel structure joined by a slit. An optical image of the relevant region of the graphene device is shown in Fig. 5a, where again the blue lines are etched walls that define the two channels and the slit bridging between them. Source and drain electrical contacts are located on the right and left sides of the lower channel, respectively (outside the field of view), whereas the upper channel is electrically floating. The slit allows electrons to be transferred between these two channels, either diffusively or ballistically (hydrodynamic flow is irrelevant at our measurement temperature of $T = 4$ K). Imaging of the resulting voltage distribution in the vicinity of the slit in the ballistic regime ($l_{mfp} = 3\,\mu m$, $n = 1.4 \times 10^{11}\,cm^{-2}$) shows a clear voltage drop along the lower

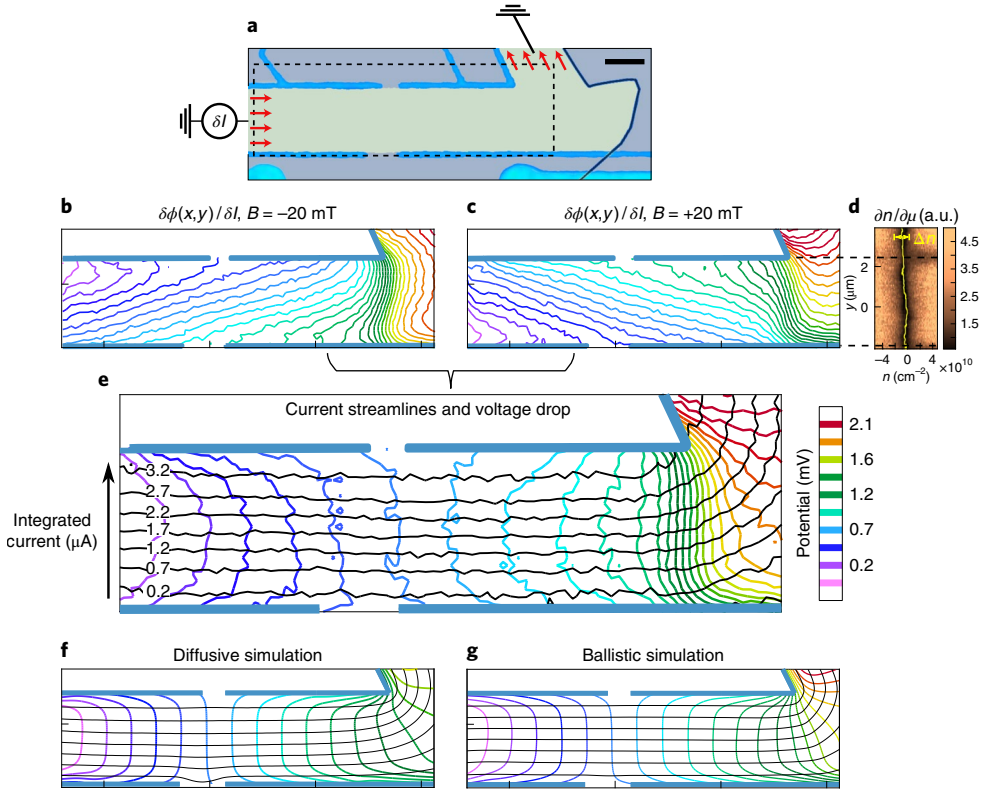

Fig. 4 | Imaging the local current density in a graphene device with a bend. a, Optical image of the device. The relevant channel is bounded by etched lines (blue) and a natural edge of the graphene (black). Irrelevant parts of the device are greyed out. The contact electrodes (beyond the field of view) inject alternating current δI at the left (red arrows) and collect it at the top (red arrows) around the bend. Scale bar, 2.5 μm. Dashed rectangle outlines the region imaged with the SET. Additional measurements near the slit opened between the flow channel and the upper chamber showed ballistic voltage patterns similar to the data presented in Fig. 5. **b**,**c**, Equipotential contours of flowing electrons at small perpendicular magnetic fields, $B = \pm 20$ mT, taken at a hole density of $n = 8.3 \times 10^{10}$ cm^{-2} set by the back-gate voltage. The magnetic field rotates the equipotential contours, allowing direct visualization of the local Hall angle. **d**, Electronic compressibility, $\partial n/\partial \mu$, measured along a line cut perpendicular to the channel (dashed line in **c**) as a function of the global density tuned by the back-gate voltage. The dark feature near zero global density corresponds to the local charge neutrality point, and its variance (yellow line) is $\delta n_{\text{disorder}} = 3 \times 10^9$ cm^{-2}, only 3% of the total density, including near the channel edge, justifying the use of a constant density in the subsequent analysis. **e**, Imaged current streamlines ψ (black iso-contours) superimposed on the zero-field voltage contours (colour). The streamlines are normalized by the Hall resistance $R_H = \frac{B}{ne}$, such that $\delta\psi(x,y) = \frac{\delta\phi_{+B}(x,y) - \delta\phi_{-B}(x,y)}{2R_H}$, which we obtain directly from the difference of the maps at positive and negative fields (**b**,**c**). The local current is given by $\mathbf{j} = \hat{z} \times \nabla(\delta\psi)$. The numbers on the black streamlines count the total integrated current from the bottom of the channel, with 0.5 μA spacing between the lines. **f**,**g**, Voltage drop and current streamlines from simulations in the diffusive regime ($\mathbf{j} = \sigma\mathbf{E}$, constant σ) and the ballistic regime (billiard ball simulation).

channel (Fig. 5b). However, on subtracting a constant background and rescaling the colour map to capture small voltage differences (Fig. 5c), we clearly resolve a distinct voltage drop in the upper channel, although curiously with its sign reversed in relation to the voltage drop in the lower channel. To directly compare between the two regions, we plot in Fig. 5e the voltage drops along line cuts in the upper and lower channels (whose positions are marked by black and green arrows in Fig. 5c). We see that in addition to the voltage drop in the upper channel being in the opposite direction to the drop in the lower channel, its magnitude is more than an order of magnitude smaller, corresponding to an electric field of 3 μV per μm for the 8 mV source-drain bias applied. When we repeat the measurement in the diffusive flow regime (Fig. 5d,f) by tuning to charge neutrality, we observe the reversed behaviour: the voltage gradient in the upper channel now has the same sign as in the lower channel.

The inverted sign of the voltage gradient is a distinctive signature of ballistic flow, and is explained schematically in the insets of Fig. 5g,h that contrast the ballistic (Fig. 5g inset) and diffusive (Fig. 5h inset) regimes. In diffusive flow, Ohm's law dictates that the voltage always drops in the direction of the current. The slit allows the current to slightly expand into the upper channel, but Ohm's law forces the voltage gradient to have the same sign there as in the lower channel. The situation is fundamentally different for ballistic flow (Fig. 5g inset). Here, hot electrons entering from the left contact of the lower channel will propagate ballistically into the right side of the upper channel, carrying along their potential. Similarly, cold holes originating from the right contact of the lower channel will ballistically transmit their potential through the slit into the left side of the upper channel. The result is a potential drop along the upper channel that is opposite in sign to the drop along the lower channel. We quantitatively model this phenomenon using electron billiards simulations of ballistic flow (using the corresponding experimental $l_{\text{mfp}} = 3$ μm) and diffusive flow, shown in the main panels of Fig. 5g,h, respectively. We find an overall close match between the simulations and the experiment, capturing both the sign and magnitude of the voltage drops in each transport regime. Imaging of this distinctive ballistic effect was made possible by our technique's ability to non-invasively resolve microvolt-scale potentials.

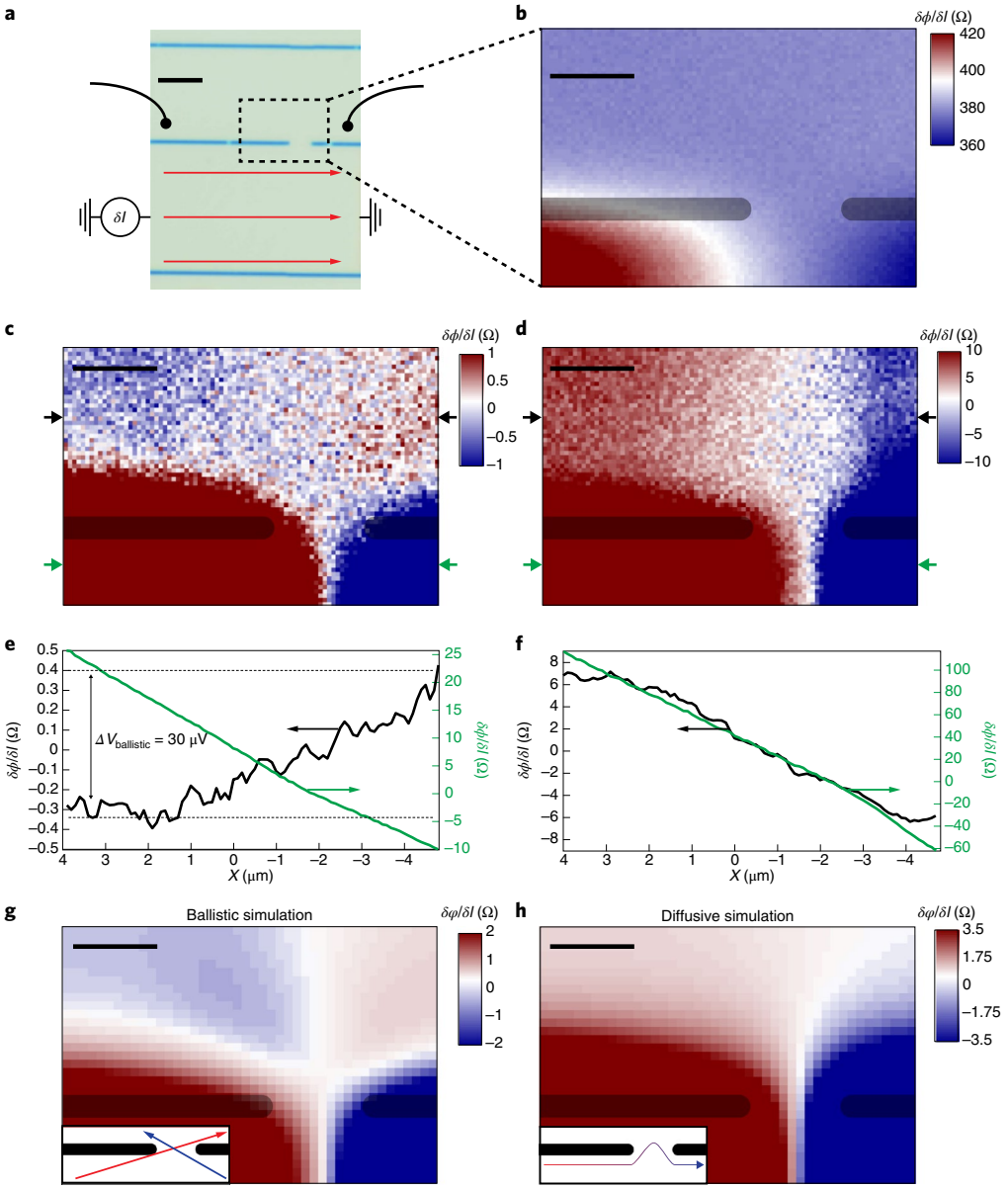

Fig. 5 | Imaging nonlocal ballistic voltage drops. a, Optical image of a graphene device, consisting of two parallel channels defined by etched lines (blue), joined by a slit. Source and drain contacts are attached to the lower channel, outside the field of view, and current is injected from left to right (red arrows). The upper channel is electrically floating, and the dashed box outlines the region imaged by the SET. Scale bar, 5 μm. **b**, Potential of flowing electrons in the vicinity of the slit, imaged in the ballistic regime, at $T = 4$ K and $n = 1.4 \times 10^{11}$ cm^{-2}. The extracted mean free path is $l_{mfp} = 3$ μm. The highlighted overlay indicates the etched walls. Compared to the scale of the voltage drop along the bottom channel, the voltage in the upper channel appears essentially constant. Scale bar is 2 μm in this and subsequent panels. **c**, Flowing electron voltage map similar to **b**, but with constant background subtracted and the colour map rescaled, showing a potential drop in the upper channel that, compared to the lower channel, is greatly reduced in magnitude and opposite in sign. **d**, Potential map of flowing electrons in the diffusive regime ($T = 4$ K, imaged at charge neutrality), with constant background subtracted and colour map scaled to show voltage drop along the upper channel, which is in the same direction as the drop along the lower channel. **e**, Voltage drop along line cuts in the lower and upper channels in **c** (ballistic regime). The voltage drop along the lower (upper) channel is plotted in green (black), and corresponds to the line cut marked by the green (black) arrows in **c**. The upper and lower channel voltage gradients clearly have opposite signs. The total voltage drop along the upper channel is $\Delta V_{ballistic} = 30$ μV, which is beyond the sensitivity of conventional imaging techniques. **f**, Similar line cuts with identical positions as in **e**, but now corresponding to the map in **d** (diffusive regime). Here, the voltage gradients in the upper and lower channels have the same sign. **g**, Electron billiards simulation of ballistic voltage map, using the experimentally determined mean free path $l_{mfp} = 3$ μm, and convolved with the SET point spread function. The simulation matches well the experimentally imaged map of **c**, capturing the differing sign of the voltage gradient between the lower and upper channels. Inset, schematic diagram explaining the origin of negative nonlocal ballistic voltage drop. In the ballistic regime, hot electrons propagate in straight line trajectories from the left side of the lower channel into the right side of the upper channel, while cold holes propagate from the right side of the lower channel into the left side of the upper channel. This results in a voltage drop in the upper channel that is reversed in sign with respect to the lower channel. **h**, Finite element simulation of diffusive voltage map, convolved with SET point spread function. The observed map matches overall the experimental data in **d**. Inset, schematic diagram explaining diffusive voltage drop. In the diffusive regime, hot electrons that originate in the left side of the lower channel flow to the right, bleeding into the upper channel through the slit and losing momentum along the way. Because the diffusive regime is governed by Ohm's law, the voltage drop must be in the direction of the current flow, and is therefore in the same direction in both the upper and lower channels.

Performance benchmarking and applicability

In the above measurements, we achieved a voltage sensitivity of $\sim 2\,\mu V\,Hz^{-1/2}$ (Supplementary Information 4). While these measurements were performed at $T = 4\,K$, we have imaged flows from cryogenic temperatures all the way to room temperature (Supplementary Information 7 and 8). The technique also functions over a large range of magnetic fields (>10 T), as transport through the SET is only weakly field dependent. We also stress that because no charge is directly transferred between the SET and the sample, buried structures impose no measurement restrictions (excluding those beneath conducting gates). Our measurements reached a spatial resolution of ~100 nm (Supplementary Information 1), limited by the lithographic dimension of the SET and its height above the sample. In principle, these values may be scaled down to obtain a resolution in the range of a few tens of nanometres. Moreover, in contrast to tip-based capacitive probes, our SET is embedded in a planar geometry surrounded by screening electrodes, resulting in an exponentially localized point spread function (Supplementary Information 1), which is crucial for resolving fine local features in a large background. We characterize the invasiveness of the SET by measuring how strongly it gates the sample under study, and find the induced local density variation to be $\delta n_{\mathrm{invasiveness}} \approx 1 \times 10^9 \mathrm{cm}^{-2}$, which is smaller than the influence of disorder (Supplementary Information 2), making its effect negligible. We have also achieved similar non-invasive voltage imaging using a scanning graphene device, albeit with reduced sensitivity (Supplementary Information 3).

The current imaging sensitivity is directly related to the voltage sensitivity via the Hall resistivity. While the SET can operate at any magnetic field, imaging unperturbed ballistic current requires the use of only a small probing field that does not affect the electron trajectories, namely, $W \ll r_C$ (where $r_C = \hbar\sqrt{\pi n}\,/\,eB$ is the cyclotron radius). The resulting sensitivity in measurements of the current density is about $10\ \mathrm{nA\ \mu m^{-1}\ Hz^{-1/2}} \times \sqrt{\frac{n}{10^{11}\mathrm{cm}^{-2}}}$. For metallic samples (for example, $n = 10^{15}\,\mathrm{cm}^{-2}$) this is comparable to the sensitivity of the present scanning SQUIDs and nitrogen vacancy centres. For typical densities in semiconductors and semimetals (for example, $n = 10^{11}\,\mathrm{cm}^{-2}$), our sensitivity is better by two orders of magnitude. Since our current imaging technique relies on Hall voltages, we are restricted from imaging supercurrents due to the compensating flow of holes along with the electrons. However, because our technique does not require deconvolution of an imaged magnetic field that can be highly nonlocal, we can otherwise easily obtain quantitative maps of current flows, especially when the current has a non-trivial profile in channels, making it very useful for deciphering non-diffusive flow regimes.

Conclusions

We have introduced a scanning SET-based method for visualizing both the voltage drop and current density of flowing electrons in two-dimensional systems, with high sensitivity and minimal invasiveness. Applying this technique to high-mobility graphene/hBN devices, we are able to spatially image the voltage drop of flowing electrons spanning from diffusive to ballistic flow. With the addition of a weak magnetic field, we further image the local current density, thus performing a complete local characterization of electron flow in a ballistic system. This technique holds promise for imaging an array of phenomena presently under intense focus, such as hydrodynamic electron flow, Dirac electron optics and Andreev reflections in magnetic field. In a more practical direction, the technique is well suited for fully characterizing transport effects due to disorder and other scattering mechanisms in a broad class of novel materials and devices, where imaging the local electronic flow patterns can provide crucial information that is otherwise inaccessible via conventional methods.

Online content

Any methods, additional references, Nature Research reporting summaries, source data, statements of data availability and associated accession codes are available at https://doi.org/10.1038/s41565-019-0398-x.

Received: 14 August 2018; Accepted: 31 January 2019;
Published online: 11 March 2019

References

1. Beenakker, C. W. J. & van Houten, H. Quantum transport in semiconductor nanostructures. *Solid State Phys. Adv. Res. Appl.* **44**, 1–228 (1991).
2. Hasan, M. Z. & Kane, C. L. Colloquium: topological insulators. *Rev. Mod. Phys.* **82**, 3045–3067 (2010).
3. Qi, X.-L. & Zhang, S.-C. Topological insulators and superconductors. *Rev. Mod. Phys.* **83**, 1057–1110 (2011).
4. Lucas, A. & Fong, K. C. Hydrodynamics of electrons in graphene. *J. Phys. Condens. Matter* **30**, 053001 (2018).
5. Landauer, R. Conductance determined by transmission: probes and quantised constriction resistance. *J. Phys. Condens. Matter* **1**, 8099–8110 (1989).
6. McLennan, M. J., Lee, Y. & Datta, S. Voltage drop in mesoscopic systems: a numerical study using a quantum kinetic equation. *Phys. Rev. B* **43**, 13846–13884 (1991).
7. Datta, S. *Electron Transport Mesoscopic System* (Cambridge Univ. Press, 1997).
8. Muralt, P. & Pohl, D. W. Scanning tunneling potentiometry. *Appl. Phys. Lett.* **48**, 514–516 (1986).
9. McCormick, K. L. et al. Scanned potential microscopy of edge and bulk currents in the quantum Hall regime. *Phys. Rev. B* **59**, 4654–4657 (1999).
10. Bachtold, A. et al. Scanned probe microscopy of electronic transport in carbon nanotubes. *Phys. Rev. Lett.* **84**, 6082–6085 (2000).
11. Weitz, P., Ahlswede, E., Weis, J., Klitzing, K. V. & Eberl, K. Hall-potential investigations under quantum Hall conditions using scanning force microscopy. *Phys. E* **6**, 247–250 (2000).
12. Melitz, W., Shen, J., Kummel, A. C. & Lee, S. Kelvin probe force microscopy and its application. *Surf. Sci. Rep.* **66**, 1–27 (2011).
13. Roth, B. J., Sepulveda, N. G. & Wikswo, J. P. Using a magnetometer to image a two-dimensional current distribution. *J. Appl. Phys.* **65**, 361–372 (1989).
14. Tokura, Y., Honda, T., Tsubaki, K. & Tarucha, S. Noninvasive determination of the ballistic-electron current distribution. *Phys. Rev. B* **54**, 1947–1952 (1996).
15. Huber, M. E. et al. Gradiometric micro-SQUID susceptometer for scanning measurements of mesoscopic samples. *Rev. Sci. Instrum.* **79**, 053704 (2008).
16. Rondin, L. et al. Magnetometry with nitrogen-vacancy defects in diamond. *Rep. Prog. Phys.* **77**, 056503 (2014).
17. Tetienne, J.-P. et al. Quantum imaging of current flow in graphene. *Sci. Adv.* **3**, e1602429 (2017).
18. Chang, K., Eichler, A., Rhensius, J., Lorenzelli, L. & Degen, C. L. Nanoscale imaging of current density with a single-spin magnetometer. *Nano Lett.* **17**, 2367–2373 (2017).
19. Vasyukov, D. et al. A scanning superconducting quantum interference device with single electron spin sensitivity. *Nat. Nanotechnol.* **8**, 639–644 (2013).
20. Eriksson, M. A. et al. Cryogenic scanning probe characterization of semiconductor nanostructures. *Appl. Phys. Lett.* **69**, 671–673 (1996).
21. Bhandari, S. et al. Imaging cyclotron orbits of electrons in graphene. *Nano Lett.* **16**, 1690–1694 (2016).
22. Fei, Z. et al. Gate-tuning of graphene plasmons revealed by infrared nano-imaging. *Nature* **487**, 82–85 (2012).
23. Chen, J. et al. Optical nano-imaging of gate-tunable graphene plasmons. *Nature* **487**, 77–81 (2012).
24. Mueller, T., Xia, F., Freitag, M., Tsang, J. & Avouris, P. Role of contacts in graphene transistors: a scanning photocurrent study. *Phys. Rev. B* **79**, 245430 (2009).
25. Fontein, P. F. et al. Spatial potential distribution in GaAs/$Al_xGa_{1-x}As$ heterostructures under quantum Hall conditions studied with the linear electro-optic effect. *Phys. Rev. B* **43**, 12090–12093 (1991).
26. Knott, R., Dietsche, W., v. Klitzing, K., Eberl, K. & Ploog, K. Inside a 2D electron system: images of potential and dissipation. *Solid. State. Electron.* **37**, 689–692 (1994).
27. Gao, C., Wei, T., Duewer, F., Lu, Y. & Xiang, X. D. High spatial resolution quantitative microwave impedance microscopy by a scanning tip microwave near-field microscope. *Appl. Phys. Lett.* **71**, 1872–1874 (1997).
28. Wang, Z. et al. Quantitative measurement of sheet resistance by evanescent microwave probe. *Appl. Phys. Lett.* **86**, 153118 (2005).
29. Yoo, M. J. et al. Scanning single-electron transistor microscopy: imaging individual charges. *Science* **276**, 579–582 (1997).

30. Ilani, S. et al. The microscopic nature of localization in the quantum Hall effect. *Nature* **427**, 328–332 (2004).
31. Honig, M. et al. Local electrostatic imaging of striped domain order in $LaAlO_3/SrTiO_3$. *Nat. Mater.* **12**, 1112–1118 (2013).
32. Yacoby, A., Hess, H. F., Fulton, T. A., Pfeiffer, L. N. & West, K. W. Electrical imaging of the quantum Hall state. *Solid State Commun.* **111**, 1–13 (1999).
33. Waissman, J. et al. Realization of pristine and locally tunable one-dimensional electron systems in carbon nanotubes. *Nat. Nanotechnol.* **8**, 569–574 (2013).
34. Ben Shalom, M. et al. Quantum oscillations of the critical current and high-field superconducting proximity in ballistic graphene. *Nat. Phys.* **12**, 318–322 (2016).
35. Levinson, I. B. Potential distribution in a quantum point contact. *Sov. Phys. JETP* **68**, 1257–1265 (1989).
36. Xia, F., Perebeinos, V., Lin, Y. M., Wu, Y. & Avouris, P. The origins and limits of metal-graphene junction resistance. *Nat. Nanotechnol.* **6**, 179–184 (2011).
37. Yu, Y. J. et al. Tuning the graphene work function by electric field effect. *Nano Lett.* **9**, 3430–3434 (2009).
38. Morikawa, S. et al. Imaging ballistic carrier trajectories in graphene using scanning gate microscopy. *Appl. Phys. Lett.* **107**, 243102 (2015).
39. Bhandari, S. et al. Imaging electron flow from collimating contacts in graphene. *2D Mater.* **5**, 021003 (2018).
40. Tarucha, S., Saku, T., Tokura, Y. & Hirayama, Y. Sharvin resistance and its breakdown observed in long ballistic channels. *Phys. Rev. B* **47**, 4064–4067 (1993).
41. Falkovich, G. & Levitov, L. Linking spatial distributions of potential and current in viscous electronics. *Phys. Rev. Lett.* **119**, 066601 (2017).

Acknowledgements

We thank G. Falkovich, L. Levitov, A. Shytov and A. Stern for discussions and D. Mahalu for electron-beam lithography. We further acknowledge support from the Helmsley Charitable Trust grant, the ISF (grant no. 712539), WIS-UK collaboration grant and the ERC-Cog (See-1D-Qmatter, no. 647413).

Author contributions

L.E., S.I. and J.A.S. conceived the technique. L.E., A.R., S.I. and J.A.S. created the SETs, performed the measurements and analysed the data. J.B., D.P., J.Z. and M.B.-S. fabricated the graphene devices. K.W. and T.T. supplied the hBN crystals. L.E., S.I. and J.A.S. wrote the manuscript with input from all authors.

Competing interests

The authors declare no competing interests.

Additional information

Supplementary information is available for this paper at https://doi.org/10.1038/s41565-019-0398-x.

Reprints and permissions information is available at www.nature.com/reprints.

Correspondence and requests for materials should be addressed to J.A.S.

Journal peer review information*Nature Nanotechnology* thanks Klaus Ensslin and other anonymous reviewer(s) for their contribution to the peer review of this work.

Publisher's note: Springer Nature remains neutral with regard to jurisdictional claims in published maps and institutional affiliations.

Methods

Device fabrication. Scanning SET devices were fabricated using our nano-assembly technique, presented in detail in ref. [33]. The graphene/hBN devices were fabricated using electron-beam lithography and standard microfabrication procedures[34].

Measurements. The measurements are performed in a home-built, variable temperature, Attocube-based scanning probe microscope. The microscope operates in vacuum inside a liquid helium dewar with a superconducting magnet, as well as under ambient conditions. The measurement apparatus is mechanically stabilized using Newport laminar flow isolators. For variable temperature studies, a local resistive heater is used to heat the sample under study from $T = 4$ K up to room temperature. A DT-670 diode thermometer chip is mounted proximal to the sample and on the same printed circuit board for precise temperature control. Voltages and currents (for both the SET and sample under study) are sourced using a home-built digital–analogue converter array, and measured using a home-built, software-based audio-frequency lock-in amplifier consisting of a Femto DPLCA-200 current amplifier and NI-9239 analogue–digital converter. The local gate voltage of the SET is dynamically adjusted via custom feedback electronics employing a least squares regression algorithm to prevent disruption of the SET's working point during scanning and ensure reliable measurements.

Data availability

The data that support the plots and other analysis in this work are available from the corresponding author upon request.